Mohamed Atef Hassan, Michal Kern, Anh Chu, Gatik Kalra, Ekaterina Shabratova, Aleksei Tsarapkin, Neil MacKinnon, Klaus Lips, Christian Teutloff, Robert Bittl, Jan Gerrit Korvink and Jens Anders*

Towards single-cell pulsed EPR using VCO-based EPR-on-a-chip detectors

Abstract: Electron paramagnetic resonance (EPR) is the gold standard for studying paramagnetic species. As an example, in structural biology, it allows to extract information about distance distributions on the nanometer scale via site-directed spin labeling. Conventional pulsed EPR of biological samples is currently limited to relatively large sample concentrations and cryogenic temperatures, mainly due to low sensitivity and the significant dead time associated with conventional resonator-based EPR setups, essentially precluding in-cell EPR under physiological conditions. This paper presents our latest progress toward single-cell pulsed EPR using VCO-based EPR-on-a-chip (EPRoC) sensors. Together with an analytical model for VCO-based pulsed EPR, we present an experimental scheme to perform dead-time-free pulsed EPR measurements using EPRoC detectors. The proposed scheme is validated using extensive numerical simulations and proof-of-concept experiments on the spin dynamics of an organic radical at room temperature using a custom-designed EPRoC detector operating in the Ka-band around 30.4 GHz. Additionally, we discuss methods to improve the excitation field homogeneity and sample handling through chip post-processing and custom-designed microfluidics. Finally, we present our progress towards compact, portable pulsed EPR spectrometers incorporating EPRoC detectors, microfluidics, and custom-designed permanent magnets. Such portable EPR spectrometers can pave the way toward new EPR applications, including point-of-care diagnostics.

Keywords: dead time free EPR; EPR; EPR-on-a-chip; EPRoC; Rabi oscillations; VCO-based pulsed EPR.

1 Introduction

Electron paramagnetic resonance (EPR) is a widely used analytical tool that provides insight into the dynamics and structures of molecules containing unpaired electrons. The applications for EPR include quantum computing and spintronics, where EPR has been used to observe the spin dynamics in molecular qubits [1], medicine, where EPR can shine light on oxidative states and their role in Alzheimer's disease [2], structural biology, where EPR is a powerful tool for studying the structure of biomacromolecules [3] such as proteins and their folding dynamics [4], and chemistry, where EPR is, e.g. used to investigate limitations of current solid-state batteries [5]. Despite its immense analytical power, EPR is not a widely used technique. This is mainly due to instrumental limitations of the EPR spectrometers available today. Here, commercially available high-end spectrometers make use of bulky (>1 m³), heavy (≈1000 kg) electromagnets to produce large (up to 3 T) static magnetic fields B_0 and high-end electronics to provide an optimum sensitivity at high instrumental costs, frequently exceeding 1 Mio € for pulsed EPR spectrometers. In contrast, benchtop EPR spectrometers are available at a greatly reduced form factor (down to the size of a shoebox, still weighing around 100 kg) and price (around 50 k€); however, the relatively low B_0 field around 0.3 T limits the achievable sensitivity and the range of EPR experiments that can be performed with such benchtop units is restricted to classical continuous-wave

*Corresponding author: Jens Anders, Institute of Smart Sensors, University of Stuttgart, Pfaffenwaldring 47, 70569 Stuttgart, Germany; and Center for Integrated Quantum Science and Technology, Stuttgart and Ulm, Germany, E-mail: jens.anders@iis.uni-stuttgart.de
Mohamed Atef Hassan and Michal Kern, Institute of Smart Sensors, University of Stuttgart, Pfaffenwaldring 47, 70569 Stuttgart, Germany
Anh Chu, Institute of Smart Sensors, University of Stuttgart, Pfaffenwaldring 47, 70569 Stuttgart, Germany; and Center for Integrated Quantum Science and Technology, Stuttgart and Ulm, Germany
Gatik Kalra, Neil MacKinnon and Jan Gerrit Korvink, Institute of Microstructure Technology, Karlsruhe Institute of Technology, Karlsruhe, Germany
Ekaterina Shabratova and Klaus Lips, Helmholtz-Zentrum Berlin für Materialien und Energie, Department Spins in Energy Conversion and Quantum Information Science (ASPIN), Hahn-Meitner-Platz 1, 14109 Berlin, Germany
Aleksei Tsarapkin, Ferdinand-Braun-Institut gGmbH, Leibniz-Institut für Höchstfrequenztechnik, Gustav-Kirchhoff-Straße 4, 12489 Berlin, Germany
Christian Teutloff and Robert Bittl, Fachbereich Physik, Freie Universität Berlin, Arnimallee 14, 14195 Berlin, Germany

(CW) EPR measurements. A further reduction in the weight and price of conventional EPR spectrometers is prevented by the way in which conventional EPR experiments are performed, cf. Section 2, which requires powerful microwave sources, microwave resonators and waveguides in addition to bulky and power hungry electromagnets. To solve this problem, Yalcin and Boero [6] proposed the use of chip-integrated LC oscillators as EPR detectors, the so-called EPR-on-a-chip (EPRoC) detectors. In the proposed approach, the current running through the on-chip inductor produces the microwave magnetic field B_1 exciting the electron spin ensemble and the resulting change in spin magnetization is detected as a change in the frequency of the oscillator. While replacing all microwave components in the conventional EPR setup, the fixed-frequency oscillators still require a sweepable B_0 field, mandating the use of electromagnets, and, thereby, preventing a further miniaturization of the EPR experimental setup. A detailed analysis of oscillator-based EPR detectors is presented in [7], which showed that the oscillator-based detectors provide a limit of detection that is equal to that of classical resonator-based detection. As an important next step, the oscillator-based detection approach was extended by Handwerker et al. [8] by the use of voltage-controlled LC oscillators (VCOs). Such VCO-based EPRoC detectors enable wide-range frequency sweeps with near-constant sensitivity – something that is intrinsically not possible with conventional resonator-based detection – thereby, allowing to replace the power-hungry electromagnets with permanent magnets for the generation of the static field B_0. This enabled designing the world's first portable, battery-operated EPR spectrometer [8]. More recently, the VCO-based approach has been further improved by the use of arrays of injection-locked VCOs to improve the concentration sensitivity [9] and embedding the VCOs into phase-locked loops (PLLs) [10]. The latter measure is important to precisely control the VCO phase and frequency from an external reference in the presence of experimental drifts and fluctuations as well as EPR-induced frequency shifts. Moreover, very recently, the VCO-based approach has been extended from continuous-wave (CW) to rapid-scan (RS) measurements by embedding the VCO detector into an on-chip high-bandwidth (BW) PLL [11].

In this paper, we will present a method for performing pulsed EPR experiments with VCO-based EPRoC detectors together with proof-of-concept experiments. Moreover, we will present a method for post-processing the VCO-based EPRoC detectors to improve their performance in pulsed EPR and render them more suitable for *in-situ and operando* EPR. Here, although *in-situ* EPR has been reported in the literature [12, 13], both *in-situ and operando* EPR remain very difficult in conventional EPR, and

the proposed VCO-based detectors present a promising alternative.

The paper is organized as follows. In Section 2, we present the fundamentals of conventional EPR spectrometers, including pulsed mode operation. Next, in Section 3, we first discuss the operating principle of VCO-based EPR before we propose an experimental scheme for extending VCO-based EPR to pulsed measurements, including an analytical model for the expected EPR signals. In Section 4, we present numerical simulations that verify the proposed experimental scheme and analytical model. Section 5 then deals with closed-loop experimental schemes for pulsed EPR for improved robustness against environmental fluctuations. Next, in Section 6, we present proof-of-concept experimental results of VCO-based pulsed EPR using a custom-designed EPRoC detector. Sections 7 and 8 deal with techniques for improved sample placement and delivery, employing holes through the EPRoC detectors and custom-designed microfluidics. In Section 9, we present the design of a portable magnet for Ka-band EPR, before we conclude the paper with a summary and an outlook on future work in Section 10.

2 Conventional EPR detection

2.1 EPR fundamentals and continuous-wave EPR

The electron possesses an intrinsic magnetic moment, emerging from its spin angular momentum or spin. The spin magnetic moment operator has two distinct eigenvalues, corresponding to two possible energy states of the electron, which are degenerate in the absence of an external magnetic field. When the electron is placed in a static magnetic field B_0, the Zeeman effect lifts the degeneracy of these states and splits them with an energy difference ΔE according to

$$\frac{\Delta E}{\hbar} = \gamma \cdot B_0 = \omega_L, \tag{1}$$

where ω_L is the so-called Larmor frequency, $\hbar$ is the reduced Planck constant and $\gamma/2\pi \approx 28\,\text{GHz/T}$ is the electron gyromagnetic ratio. If an additional AC magnetic field $B_1 \perp B_0$ is applied to the sample, with a microwave (MW) frequency $\omega_{MW} = \omega_L$ equal to the Larmor frequency, transitions between the two energy levels occur, cf. Figure 1. The net effect of the energy level transitions can be modeled as a change in the sample's dynamic complex magnetic susceptibility $\chi = \chi' + j\chi''$ and, thus, the sample's net magnetization $M = \chi H_0 = \chi B_0/\mu_0$, where μ_0 is the
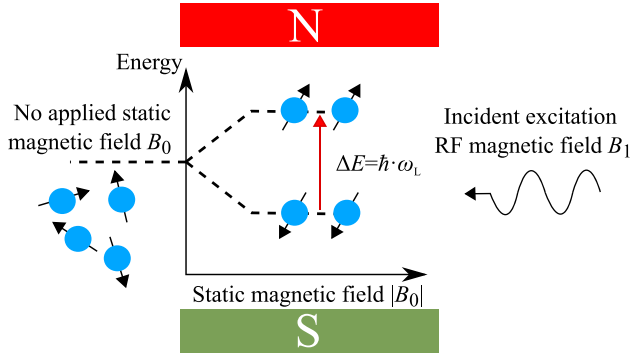
Figure 1: EPR working principle.

vacuum permeability. The real and imaginary part of χ represent the dispersion and power absorption of radiation, respectively. χ' and χ'' contain the same information and are related by the Kramers-Kronig relation.

To measure the resonant EPR transitions, samples are most commonly placed inside resonant cavities, which are tuned to a certain frequency with large quality factors (Q factors) on the order of 10^3, while sweeping the external B_0 field through the resonant condition using an electromagnet. The EPR signal is then detected as a change in the reflected power from the resonator, e.g. using a circulator, cf. Figure 2. Here, it should be noted that the EPR signal in a CW experiment, has both absorptive and dispersive components. In a conventional EPR experiment a so-called automated frequency control loop (AFC) unit [14] is used to lock the frequency of the B_1 field to the resonance frequency of the cavity as it is moving due to the EPR effect. This results in the detection of only a single component of the complex sample susceptibility, most commonly the absorption signal χ''.

A simplified block diagram of a conventional EPR spectrometer is shown in Figure 2. The microwave power is applied to the sample inside the resonator via a circulator,

and the change in reflected power is measured using an amplitude detector at the third port of the circulator. In most situations, lock-in detection is introduced to improve the SNR in the presence of low-frequency noise and drifts in the experimental setup by modulating the B_0 field using a pair of dedicated modulation coils.

2.2 Pulsed EPR

In contrast to CW EPR, in pulsed EPR, the sample is irradiated with the B_1 field for a duration that is much shorter than the sample's relaxation times, and the signal is detected as microwave (MW) emission from the resonator after the pulse. Here, the spin dynamics of a simple two-level system under MW irradiation can be described using the classical Bloch equations with a phenomenological inclusion of relaxation processes. To simplify the equations, a rotating coordinate frame of reference is commonly used, where B_0 is aligned with the z axis and the x and y axes rotate around z in a right-hand sense with the frequency ω_{MW}. In this coordinate frame, B_1 is time independent and oriented along the x axis. The transient magnetization behavior is then described by

$$\frac{dM_x}{dt} = -(\omega_L - \omega_{MW})M_y - \frac{M_x}{T_2} = -\Omega M_y - \frac{M_x}{T_2} \quad (2a)$$

$$\frac{dM_y}{dt} = (\omega_L - \omega_{MW})M_x - \gamma B_1 M_z - \frac{M_y}{T_2}$$

$$= \Omega M_x + \omega_1 M_z - \frac{M_y}{T_2} \quad (2b)$$

$$\frac{dM_z}{dt} = \gamma B_1 M_y - \frac{M_z^0 - M_z}{T_1} = \omega_1 M_y - \frac{M_z^0 - M_z}{T_1}, \quad (2c)$$

where $\Omega = \omega_L - \omega_{MW}$ is referred to as resonance offset, $\omega_1 = -\gamma B_1$ is the so-called nutation frequency, and T_1, T_2 are the
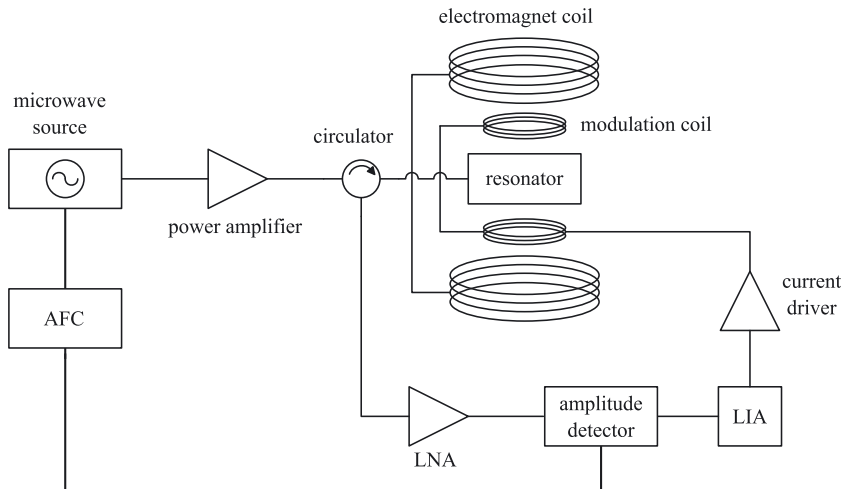

Figure 2: A conventional CW-EPR spectrometer.

longitudinal and transversal relaxation times, respectively [14]. MW emission is related to electron coherence, which manifests as the transverse magnetization $M_x - jM_y$, precessing at a frequency of ω_L in the xy plane of the static laboratory frame. In conventional pulsed EPR experiments, the setup of Figure 3 is used to detect the precessing spin magnetization [14]. Here, the microwave signal is typically generated by a klystron or a Gunn diode. The MW source is followed by a pulse shaping unit, consisting of multiple channels with individually adjustable attenuators, phase shifters and fast MW switches with rise times between 0.5 and 2 ns The pulse patterns from multiple channels are then combined and sent to a power amplifier, commonly a traveling-wave tube (TWT) amplifier producing power levels up to 1 kW, which are then optionally attenuated and sent to the sample-containing resonator through a circulator. Typical resonators used in EPR are split-ring and dielectric resonators with Q values of up to 10,000. The Q value is usually adjusted by changing the coupling to the resonator, in order to control the ringdown after each excitation pulse as required by the experiment. After the excitation pulse, the transient EPR signal with typical power levels between nW and μW, is directed by the circulator to a low-noise preamplifier. During the excitation pulse, the LNA is protected by a fast MW switch. The amplified signal is then fed to a quadrature mixer, where it is frequency downconverted with the excitation signal, and digitized. Importantly, the relatively large power levels that have to be applied to conventional resonators to produce the required B_1 field strength for short pulses prevent a detection of the EPR signal during the pulse and lead to significant dead times (around 50–100 ns for typical resonators) after the pulse.

3 VCO-based EPR

In VCO-based EPR, the B_1 field required to excite the electron spin ensemble is produced by the current running through the tank inductor of a chip-integrated LC oscillator. The resulting change in sample magnetization produces a change in the VCO's amplitude and frequency, which can be conveniently demodulated and frequency downconverted on-chip, in principle, removing the need for any additional MW components in the experimental setup. This basic working principle of VCO-based EPR is illustrated in Figure 4a.

3.1 Continuous-wave measurements using VCOs

In CW EPR experiments, the change in sample magnetization can be modeled as an equivalent change in the tank coil's inductance and resistance according to [15]

$$L_{tot} = L_0 + L_{spin} \approx L_0 \cdot (1 + \chi' \cdot \eta) \tag{3a}$$

$$R_{tot} = R_0 + R_{spin} \approx R_0 - \chi'' \eta \cdot \omega_{MW} \cdot L_0$$
$$= R_0 \cdot (1 - \chi'' \cdot \eta \cdot Q_{coil}), \tag{3b}$$

where χ' and χ'' are the real and imaginary parts of the complex sample susceptibility, respectively, η is the so-called fill factor, indicating how much of the total sensitive coil volume is filled with the EPR sample, L_0 and R_0 are the tank inductance and resistance in the absence of EPR, Q_{coil} is the Q factor of the tank inductor, and ω_{MW} is the frequency of the microwave B_1 field. For a cross-coupled pair LC VCO, this change in the effective coil inductance and resistance leads to a corresponding change in the VCO's frequency and amplitude according to [15, 16]

$$\Delta\omega_{osc,\,spin} \approx -\frac{1}{2} \cdot \omega_{osc,\,0} \cdot \eta \cdot \chi' \tag{4a}$$

$$\Delta A_{osc,\,spin} \approx A_{osc,\,0} \cdot \frac{Q_{coil}}{2 \cdot (\alpha_{od} - 1)} \cdot \eta \cdot \chi'', \tag{4b}$$

where $\omega_{osc,0}$ and $A_{osc,0}$ are the oscillation frequency and amplitude, respectively, in the absence of EPR, Q_{coil} is the
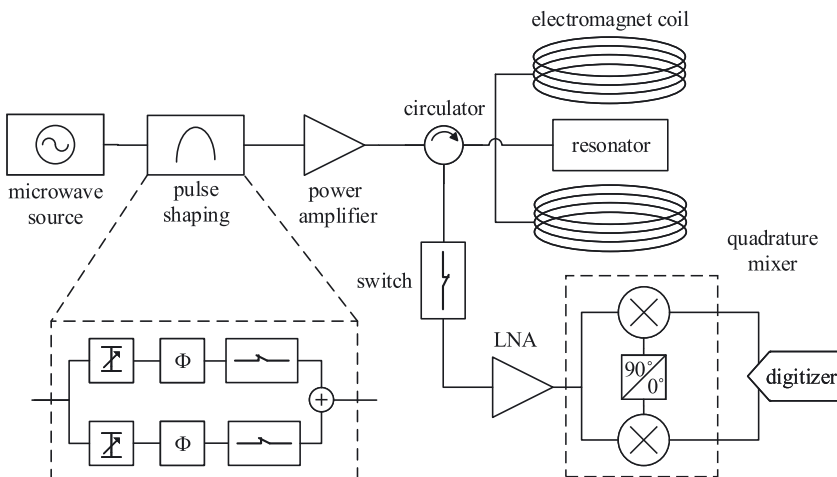

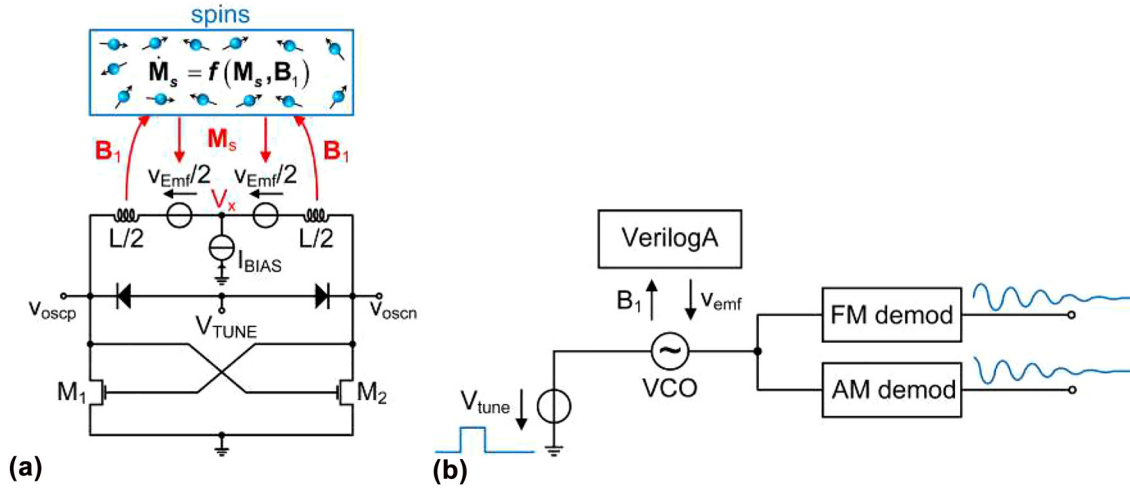**Figure 3:** Conventional pulse-EPR spectrometer.

Figure 4: (a) Equivalent circuit model of the interaction between a spin ensemble and a VCO. (b) The simulation setup used to simulate open-loop pulsed VCO-based EPR experiments in Cadence Virtuoso.

quality factor of the tank inductor and α_{od} is a parameter indicating by how much the negative transconductance produced by the cross-coupled pair is larger than the equivalent parallel coil conductance, cf [16]. A VCO-based CW EPR experiment can be performed by either sweeping the B_0 field for a fixed VCO frequency or sweeping the VCO frequency for a fixed value of B_0, the latter enabling the use of permanent magnets as source for the B_0 field. Overall, in VCO-based CW EPR experiments, the real part of the complex susceptibility (dispersion spectrum) mostly affects the VCO's frequency, while the imaginary part of χ dominantly affects the amplitude of oscillation. In order to extract the EPR information from the output voltage of the VCO, proper frequency and amplitude demodulation are required. Lock-in detection can conveniently be introduced by frequency modulation via the VCO tuning voltage.

3.2 Pulsed EPR measurements using VCOs

So far almost all VCO-based EPR experiments presented in the literature have been conducted in the CW mode of operation, the only exceptions being the recent rapid scan experiments presented in [11, 17, 18]. In order to understand the interaction of the VCO and the electron spin ensemble during and after a pulsed excitation, the steady-state model discussed in the previous section is not sufficient. A suitable equivalent circuit model is shown in Figure 4a, where the precessing spin magnetization is modeled as an electromotive force (emf) induced in the tank coil. Said emf can be calculated from an energy consideration similar to the approach used in [15] according to

$$v_{emf}(t) = -\frac{d}{dt} \int_{V_s} \vec{B}_u \cdot \vec{M}_{spin} dV, \qquad (5)$$

where V_s is the sample volume, $\vec{B}_u$ is the unitary magnetic field of the tank inductor, and $\vec{M}_{spin}$ is the spin magnetization. The emf given by eq. (5), in turn, produces a modulation of the amplitude and the frequency of the VCO output voltage. In order to quantify the resulting FM and AM components, we have performed a nonlinear perturbation analysis of a cross-coupled LC tank oscillator, resulting in the following approximate expressions for the FM and AM components, respectively:

$$\Delta\omega_{osc,spin}(t) \approx \frac{\omega_{osc,0}}{A_{osc,0}} \cdot \cos(\omega_{osc,0}t) \cdot \frac{d}{dt} \int_{V_s} \vec{B}_u \cdot \vec{M}_{spin} dV \quad (6a)$$

$$\Delta A_{osc,spin}(t) \approx \frac{Q_{coil}}{\alpha_{od}-1} \cdot \sin(\omega_{osc,0}t)$$

$$\cdot \frac{d}{dt} \int_{V_s} \vec{B}_u \cdot \vec{M}_{spin} dV, \qquad (6b)$$

where all quantities are defined according to Section 3.1 and eq. (5). Here, it should be noted that there is a small (second-order) coupling between the EPR-induced frequency $\Delta\omega_{osc,spin}(t)$ and amplitude changes $\Delta A_{osc,spin}(t)$, which has been ignored for simplicity in eq. (6). According to eq. (6), the EPR-induced amplitude and frequency shifts are in quadrature with respect to each other, and they both individually contain the complete information on the precessing spin magnetization $\vec{M}_{spin}$. Since the information on the spin magnetization is contained in the frequency and amplitude of the VCO, FM and AM demodulation, respectively, are required to extract this information from the VCO output voltage.

Overall, the discussion above clearly shows that the detection of transient/pulsed EPR signals is possible with VCO-based detectors, the detection concept being distinctly different from conventional EPR. More specifically, in conventional EPR, the reflected signal from the resonator contains the EPR signal in its amplitude and phase, the amplitude and phase directly representing the amplitude and phase of the spin magnetization, requiring no further demodulation. By contrast, in VCO-based EPR, the spin magnetization produces an amplitude and frequency modulation of a carrier given by the VCO's natural frequency, i.e. its frequency in the absence of EPR, mandating a dedicated AM and FM step to extract the information on the spin magnetization.

In the following, we will explain that also a pulsed excitation is possible using VCOs, again highlighting the difference to conventional pulsed EPR. The major difference in VCO-based pulsed EPR originates from the fact that an oscillator has a certain minimum oscillation amplitude below which the oscillator ceases to operate properly. Therefore, when switching the oscillator off, the VCO-based detector mostly becomes a conventional resonator-based detector with a corresponding ringdown at the end of the excitation pulse, i.e. providing no advantage compared to a conventional resonator in terms of dead time after the pulse. Moreover, when the oscillator is turned back on, it displays a relatively long start-up behavior, which would produce effective pulse widths that are potentially varying in length and, therefore, are hard-to-predict in practice. Consequently, it is in general not possible to produce a reliable EPR excitation pulse by modulating the VCO's amplitude from 'off' to 'on' and back to 'off'. This is illustrated by the simulation results in Figure 5a. According to the figure, there is a startup behavior that causes a delay between the pulse control signal (red) and the beginning of the effective EPR pulse (blue) and a noticeable ringdown after the end of the

control pulse (black envelope). Therefore, instead of modulating the VCO's amplitude, we propose to use a switching of the VCO's frequency from an off-resonance value $\omega_L + \Delta\omega_{off}$ to an on-resonance value ω_L and back to produce a pulsed excitation, cf. Figure 5b. In this way, the oscillator is continuously running, removing the oscillator's unpredictable start-up behavior as well as the ringdown after the excitation pulse. According to the simulation results of Figure 5b, in this setting, the effective pulsed excitation produced by the VCO can closely follow the control pulse. By choosing the difference between the on- and off-resonance frequency $\Delta\omega_{off}$ larger than the bandwidth of the EPR spectrum under investigation, an undesirable excitation between the pulses can be avoided. An important advantages of the proposed scheme is the fact that the detector is continuously running, enabling a dead time-free detection of the EPR signal after the pulse. This is one of the most important difference between VCO-based and conventional pulsed EPR employing a resonator. More specifically, when switching off the excitation signal in conventional EPR, the energy associated with the EPR pulse needs to be removed from the resonator before the LNA can be connected to the resonator output without a risk of damaging the LNA. Since the so-called ringdown of the energy inside the resonator takes precisely Q cycles of the resonator's resonance frequency, Q being the resonator quality factor, there is a strong trade-off between sensitivity (favoring large Q factors) and dead time after the pulse (favoring low Q factors). By contrast, switching the frequency of oscillation of a VCO can be performed almost instantaneously (a second order perturbation analysis of the VCO revealed negligible inertia in the frequency switching within the oscillator), the eventual transition speed being limited either by the bandwidth of the utilized varactor and/or the source driving the VCO tuning voltage. Intuitively, there is no inertia in switching
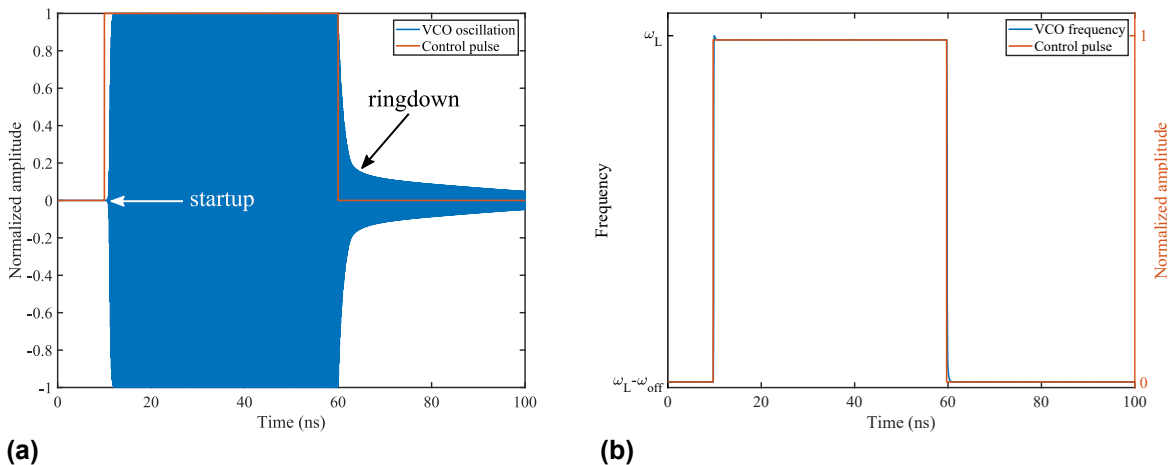

(a) **(b)**

Figure 5: Comparison between amplitude switching and frequency switching in VCO-based EPR. (a) Amplitude pulse. (b) Frequency pulse.

the VCO's frequency because the energy does not have to be removed from the LC tank but it is rather shifted to a different frequency. Here, it should be noted that, if the amplitude of oscillation is different at the off-resonance frequency, the process of adjusting said amplitude displays inertia, which is mostly visible in the VCO's AM signal.

Overall, a simple VCO-based pulsed EPR experiment can be performed by toggling the VCO's oscillation frequency from off-resonance to on-resonance and back, cf. Figure 5b, and detecting the resulting change in spin magnetization as a transient change of the VCO's frequency and amplitude.

4 VCO-based pulsed EPR: simulation results

In order to investigate the VCO-based pulsed EPR scheme proposed in the previous section, we have performed a series of simulations in Cadence Virtuoso using the model shown in Figure 4a and the testbench of Figure 4b. In our simulations, the spin ensemble is modeled as a VerilogA block containing the Bloch equations, cf. eq. (2), which accepts the B_1 field (modeled using the coil's geometry parameters and the instantaneous value of the coil current) as input parameters and which outputs the emf induced in the tank coil. This modeling approach was presented by our group for rapid scan EPR experiments in [19]. In our pulsed EPR simulations, we used the following parameters for the VCO: A free-running oscillation frequency of 16 GHz with a 400 pH tank inductor. A quality factor of the LC tank of 40 and a VCO bias current of 20 mA. The required FM and AM demodulation to extract the EPR signal have been performed separately. For the

AM signal, the implicit AM demodulation capability of the utilized current-biased LC tank VCO at node V_x in Figure 4a, cf. [16], has been used while the FM demodulation has been performed in Matlab. In the first set of simulations, we have investigated simple pulse-acquire experiments, in which we recorded the free-induction decay (FID) after a pulsed excitation corresponding to flip angles of 90 and 180°, respectively. The corresponding results are summarized in Figure 6. The small oscillations preceding the excitation pulse are a simulation artifact. According to the figure, switching the VCO frequency from an off-resonance to an on-resonance value produces the desired transversal magnetization, and the resulting FID can be observed without dead time after the pulse. Here, it should be noted that since the VCO is continuously running during the pulse, even the Rabi oscillations during the pulse can be monitored. Moreover, the quadrature nature of the FM and AM signals after the pulse predicted by eq. (6) is clearly visible in the simulated data.

As our next step, we have investigated the behavior of the VCO-based detector for two consecutive pulses with an arbitrary inter-pulse distance of $\Delta\tau$. The corresponding results are shown in Figure 7a. According to the figure, the FIDs after the consecutive pulses are in general not in phase, which presents a problem if time-domain averaging has to be used to improve the SNR. One possible solution to this problem is to adjust the distance between consecutive pulses $\Delta\tau$ such that the second pulse is in phase with the first pulse. Here, the corresponding condition for $\Delta\tau$ can be expressed as:

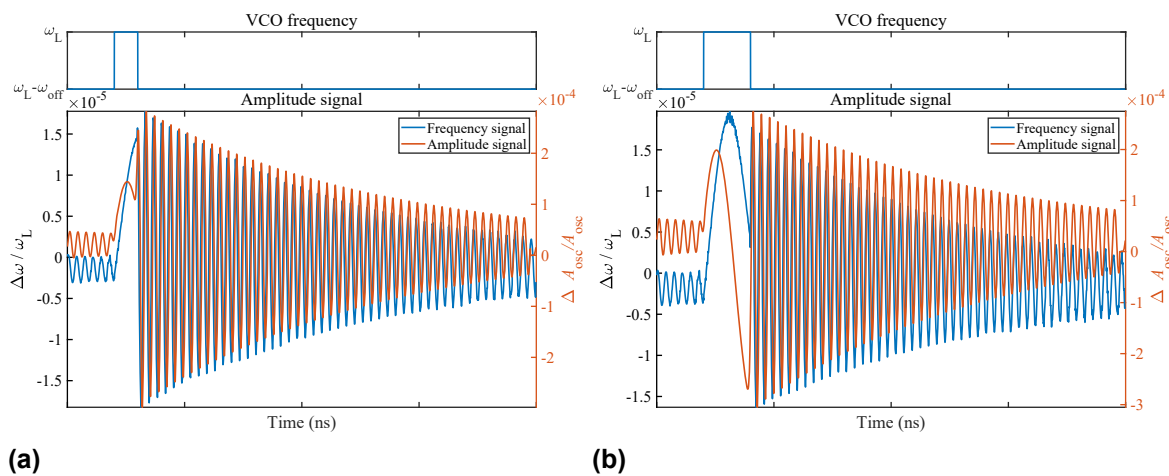$$\Delta\tau = N \cdot \frac{2\pi}{\Delta\omega_{\text{off}}}, \tag{7}$$

Figure 6: Simulations of open-loop VCO-based pulse-acquire EPR experiments. Simulation parameters: $\omega_{\text{osc},0} = 2\pi \cdot 16\,\text{GHz}$, $\omega_{\text{off}} = 2\pi \cdot 300\,\text{MHz}$. The simulated sample parameters correspond to a crystal of BDPA with $T_1 = T_2 = 100\,\text{ns}$. (a) 10 ns $\pi/2$-pulse. (b) 20 ns π-pulse.

(a)   **(b)**
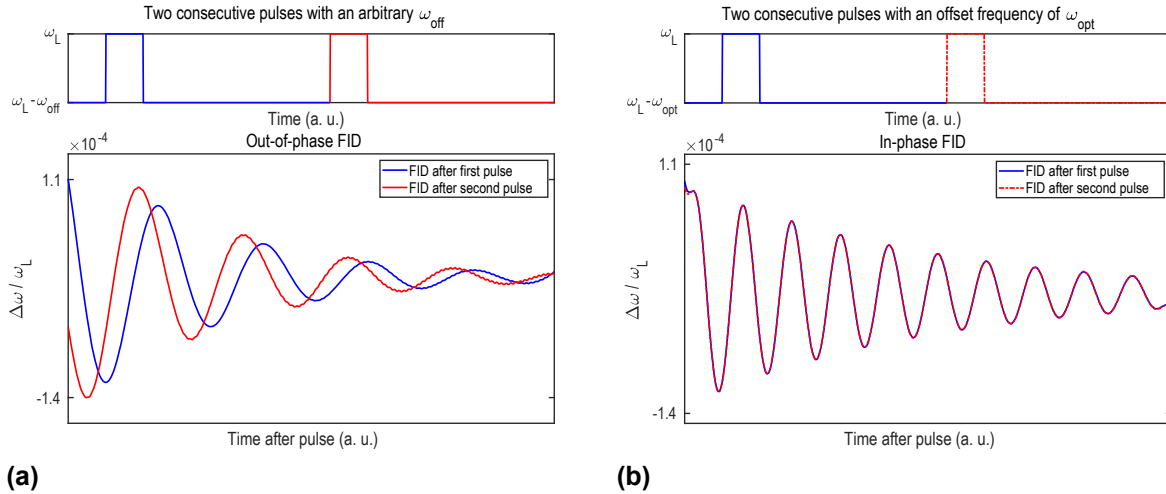
Figure 7: Two cases showing the challenge to average consecutive FIDs and the use of an optimum off-resonance frequency jump to enable averaging. (a) Two-pulse sequence showing phase mismatch between consecutive pulses when using arbitrary ω_{off}. (b) Two-pulse sequence showing phase matching between consecutive pulses when using $\omega_{\text{off}} = \omega_{\text{opt}}$ to ensure phase coherence.

where N is an integer number, and $\Delta\omega_{\text{off}}$ is the offset between the VCO frequency during the excitation pulse and the off-resonance VCO frequency after the pulse. Figure 7b shows simulation results of VCO-based pulsed EPR experiments in which the inter-pulse distance has been adjusted according to eq. (7). Clearly, the FID after consecutive pulses are now in-phase, enabling a phase-coherent averaging of consecutive FIDs to improve the SNR.

To complement our circuit simulations, we have performed quantum mechanical spin simulations using the pepper and spidyan functions of the Easyspin Matlab package [20, 21] (version 6.0.0-dev.37). In these simulations, we have modeled a spin system similar to the one that we used in the experimental section below with the following parameters: a spin of 1/2, g = 2.0026 and a homogeneous linewidth of 0.114 mT. The resulting CW EPR spectrum around B_0 = 1084.60 mT can be seen in Figure 8a. The dispersion spectrum was obtained by Hilbert transforming the absorption signal. In the figure, we have highlighted three points of interest using colored vertical lines: the exact point of resonance, corresponding to the maximum point of the absorption line and zero-crossing of the dispersion signal, as well as the two inflection points of the absorption line, corresponding to the maximum and minimum of the dispersion signal. These three points were then further investigated in simulations of the spin dynamics. The spin dynamics were calculated for a system with the same Larmor frequency as in the CW case and $T_1 = T_2 = 100$ ns. For excitation, a pulse length of 75 ns and an amplitude[1] of

3 MHz were used. The pulse was turned on at t = 100 ns followed by an observation window of 800 ns The presented absorption and dispersion time traces are the imaginary and real parts of the $\hat{S}_+$ ladder operator, respectively. In Figure 8b, we compare the simulated signal intensities for both the absorption and dispersion signal components when exciting the spins exactly on resonance. According to the figure, while a clear Rabi oscillation followed by a purely exponential FID can be observed in the absorption component, the dispersion signal is negligible. This changes when exciting the spin system at either of the two inflection points of the absorption signal. Here, the signal amplitudes of the absorption and dispersion signals become comparable and the sign of the dispersion signal depends on the sign of the offset from the resonance frequency. We confirmed this general behavior by the circuit simulations shown in Figure 9.

5 Closed-loop VCO-based EPR

The simulation results of the previous section have all been performed in the open-loop configuration of Figure 4b. While this configuration works very well in simulations and is instrumental in understanding the features of VCO-based pulsed EPR, fluctuations in the experimental conditions, including e.g. temperature fluctuations, limit its practical usability. Here, embedding the VCO's frequency and amplitude into corresponding control loops according to Figure 10 presents a possible solution. In the closed-loop setup of Figure 10, within the corresponding loop bandwidth, the EPR-induced

---

1 The spidyan function defines pulse amplitude by the corresponding nutation frequency $f_1 = \frac{\gamma}{2\pi}B_1$.
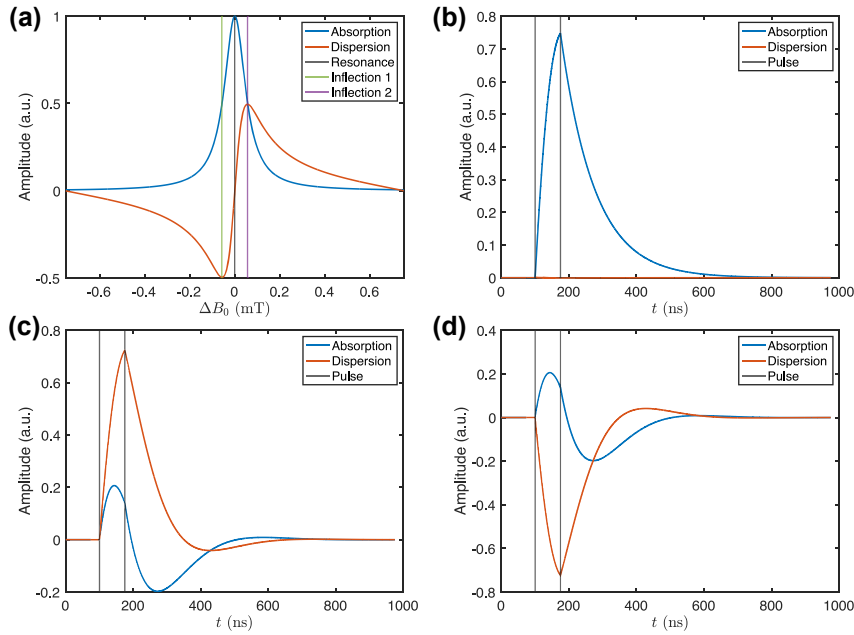
Figure 8: Simulated spin dynamics at different points of an EPR line. (a) Simulated CW-EPR spectrum with three fields of interest highlighted by the vertical lines. (b) Expected Rabi oscillations and FID signal when exciting the spin at resonance ($\Delta B_0 = 0\,\text{mT}$) with a 75 ns $\pi/2$-pulse at $t = 100$ ns. (c) Same as (b) with excitation at inflection point 1 ($\Delta B_0 = 0.057$ mT, $\Omega/2\pi = \frac{\gamma}{2\pi}\Delta B_0 = 1.6$ MHz). (d) Same as (b) with excitation at inflection point 2 ($\Omega/2\pi = -1.6$ MHz).

frequency and amplitude changes are counteracted by the corresponding loops, resulting in no net EPR-induced change of the VCO output. Instead, the FM and AM EPR signals can conveniently be extracted from the control signals of the two loops, assuming that their bandwidths are sufficiently large. Here, while CW and RS experiments [10, 11, 16] require small ($\approx$100 kHz for CW) and medium (a few tens of megahertz for RS) bandwidths, pulse experiments require a large bandwidth >>100 MHz in order to faithfully produce short (nanosecond range) excitation pulses and demodulate typical EPR spectra that easily extend over a few hundred megahertz.
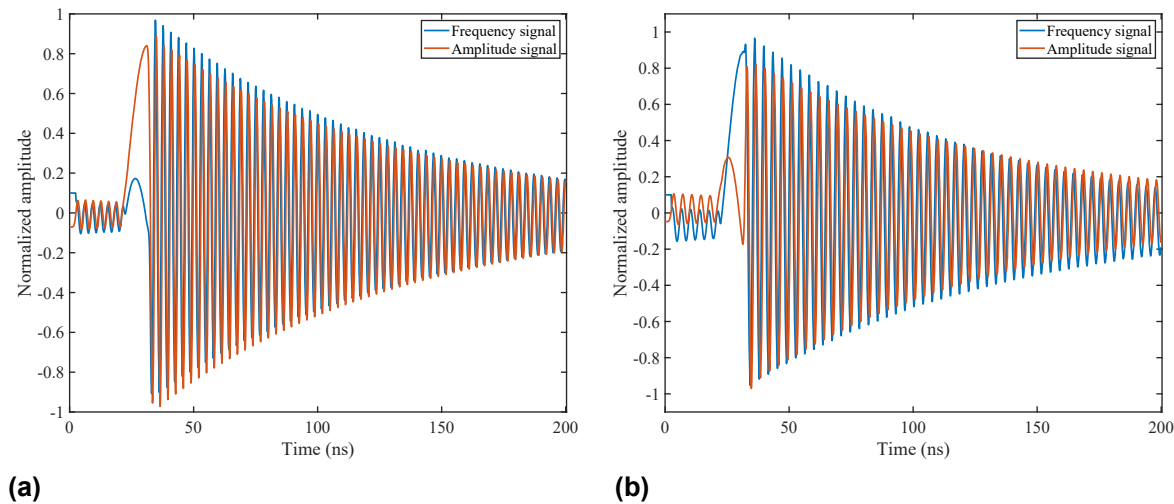

Figure 9: Circuit simulations of pulsed VCO-based EPR in an open-loop configurations at different points of an EPR line. The simulated sample is a crystal of BDPA with $T_1 = T_2 = 100$ ns. (a) On-resonance excitation: Rabi oscillations and FID signal when exciting the spin on-resonance with a 10 ns $\pi/2$-pulse at $t = 30$ ns. (b) Off-resonance excitation: Rabi oscillations and FID signal when exciting the spin off-resonance with a 10 ns $\pi/2$-pulse at $t = 30$ ns ($\Omega/2\pi = -22$ MHz).
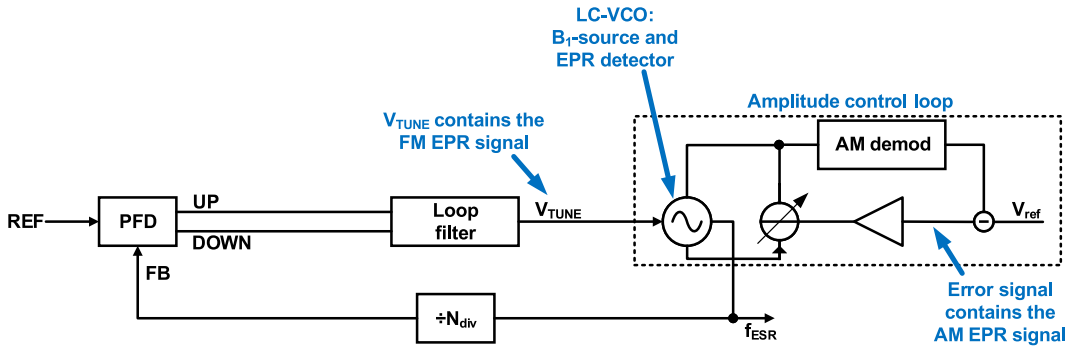
Figure 10: Illustration of the proposed close-loop setup for VCO-based EPR experiments, in which both the frequency (phase) and amplitude of the VCO are embedded into control loops.

6 VCO-based pulsed EPR: chip implementation and measurement results

In this section, we will present proof-of-concept measurement results of VCO-based pulsed EPR experiments that validate the approach for performing pulsed EPR experiments discussed in Section 3 as well as the theoretical modeling of Section 4.

6.1 Custom designed VCO-based EPRoC detectors

In order to validate the closed-loop VCO-based EPR approach discussed in Section 5, we have designed two ASICs, incorporating large bandwidth amplitude and frequency control loops. A manuscript presenting these two chips in detail is currently under preparation and, here, we will only present a short summary of the chip characteristics. The chip is manufactured in TSMC's 40 nm low-power CMOS technology. The VCO is a cross-coupled class-B oscillator operating at a center frequency of 30 GHz with a tuning range of 2.5 GHz. The varactor is divided into two sections: one for the closed-loop control and a second section enabling open-loop control of the VCO frequency. By employing a fast phase-frequency detector (PFD) operating at 1 GHz, we could design the on-chip phase-locked loop (PLL) with a large bandwidth (>200 MHz). Figure 11 shows micrographs of the two manufactured chip designs. Similar to Figure 5, the chip in Figure 11a contains both an amplitude control loop (ACL) and a PLL for closed-loop amplitude and frequency control, respectively, while the chip in Figure 11b offers only closed-loop frequency control. In both chips, the EPR signals are buffered using an on-chip low-noise high-frequency buffer with a small DC error to enable direct digitization.

6.2 Measurement results

Proof-of-concept EPR measurements were performed using the chip shown in Figure 11b and the setup of Figure 12b using a custom-designed PCB probe head inside a commercial electromagnet. To this end, a small crystal of 1,3-bisdiphenylene-2-phenylallyl:benzene complex (BDPA, purchased from Sigma Aldrich) was placed in the center of the VCO coil cf. Figure 12a. The waveforms necessary for the phase-coherent frequency jumps, cf. eq. (7), were calculated using in-house scripts and generated using a commercial arbitrary waveform generator (AWG) (Keysight M8195A). The chip output signal was digitized using a commercial digitizer
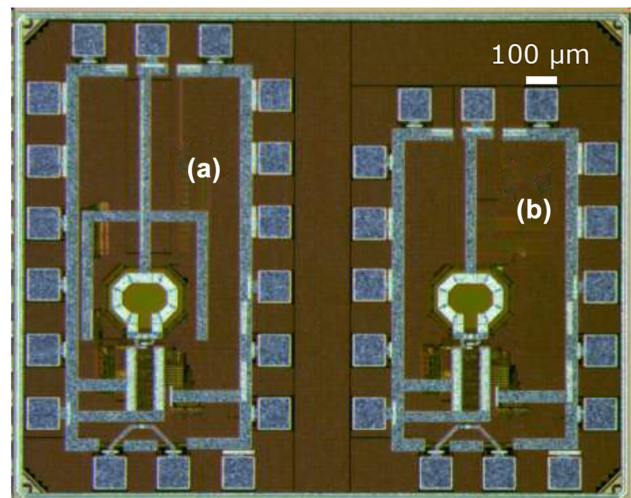

Figure 11: Micrographs of the two custom-designed EPRoC detectors: (a) closed-loop frequency control (b) closed-loop frequency and amplitude control.

(Keysight M8131A). Averaging and signal processing were performed using in-house MATLAB scripts. The pulsed measurements were performed by toggling the VCO frequency from 30.271 to 30.400 GHz ($\Delta\omega_{off}/2\pi = 129$ MHz) for 75 ns, roughly corresponding to a $\pi/2$-pulse. Averaging in the time-domain was performed by creating 10,000 subsequent pulses with an inter-pulse delay of 600 ns The data were recorded at three magnetic field values, $B_{res} + \Delta B_0$ with $B_{res} = 1084.60$ mT and two offset fields ΔB_0 corresponding to offset frequencies of $\Omega/2\pi = \frac{\gamma}{2\pi}\Delta B_0 = \{-7.2\,\text{MHz}, 0\,\text{MHz}, 7.7\,\text{MHz}\}$. To remove field-independent offsets and interferers in the chip output signal and introduced by the digitizer, we recorded data at the specified fields and a field offset by ≈ 40 mT. Then, we calculated the difference between the two data sets, and applied a digital, 5th-order, 200 MHz Butterworth low-pass filter.

The resulting time domain traces can be seen in the top graph of Figure 13. The figure also contains the corresponding excitation function (purple, right ordinate). During the pulse, which starts at $t = 100$ ns, Rabi oscillations can be observed in the traces recorded at non-zero resonance offsets Ω. By contrast, as predicted by the simulations of Section 4, close to resonance for $\Omega \approx 0$ the Rabi oscillations disappear. After the pulse, an FID is clearly observable in all three cases. Fourier transforms of the time traces are shown in the bottom part of Figure 13. For the blue trace close to resonance, the FID has a frequency of 130 MHz. For $\Omega \approx 0$, one would expect an FID frequency of $\Delta\omega_{off}/2\pi = 129$ MHz, suggesting a small resonance offset of $\Omega/2\pi \approx 1$ MHz. As predicted by the model, the FID frequency changes with the applied B_0 field, the FID frequency being given by $\omega_L + \Delta\omega_{off}$. The unequal amplitudes of the two peaks corresponding to $\Omega \neq 0$ in the bottom graph of Figure 13 can most likely be attributed to the unequal

B_0 field offsets $\Omega/2\pi = \frac{\gamma}{2\pi}\Delta B_0 = \{-7.2\,\text{MHz}, 7.7\,\text{MHz}\}$, and, more importantly, to the relatively low precision of the B_0 field, which was defined by the open-loop current of the magnet power supply. Currently, we are installing a Hall-sensor based precision field controller. Once this is probably running, we will repeat the measurements to verify whether the peak amplitudes at equal offset frequencies are equal in magnitude, as it is predicted by the theoretical model of Section 3.2.

In summary, the proof-of-concept measurements in this section have validated the proposed scheme for VCO-based pulsed EPR. Here, we could verify the possibility for pulsed
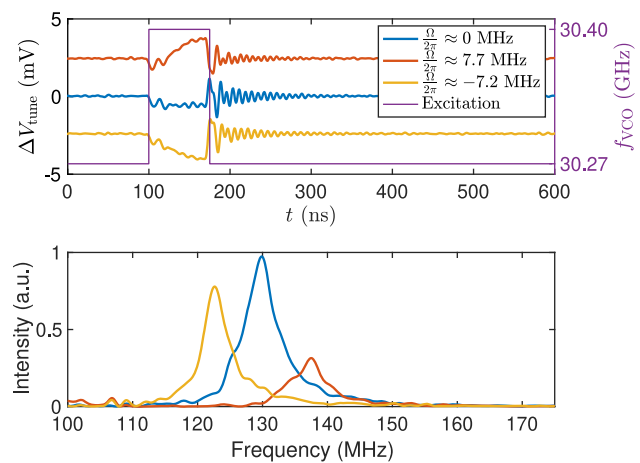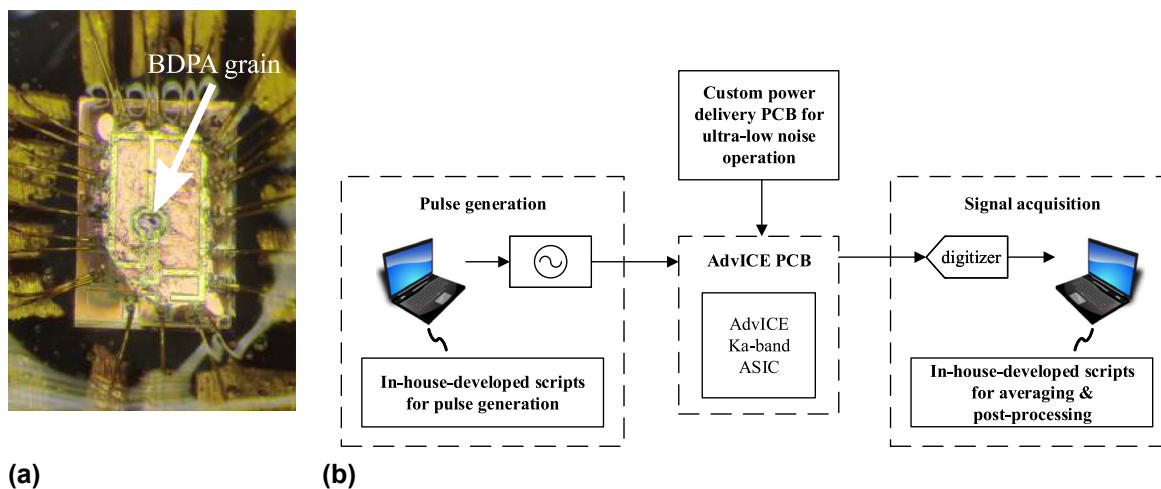

Figure 13: Proof-of-concept measurements performed at room temperature on a BDPA sample using the closed-loop measurement setup. Top: Time domain signals during and after a frequency jump at three different magnetic fields. Bottom: Fourier transformation of the time traces displayed above, showing the FID frequency change at different magnetic fields.

Figure 12: Details of the experimental setup used for the proof-of-concept experiments. (a) Bonded chip with a BDPA sample at the center of the VCO coil. (b) Block diagram of closed-loop measurements setup.

EPR measurements with a deadtime-free detection of the FID after as well as the measurement of Rabi oscillations during the excitation pulse. The experimental observations are in good agreement with the model presented in Sections 3.2 and 4, the amplitude behavior in Figure 13 requiring further investigations with a more precise B_0 field.

7 Post-processing of VCO-based EPRoC detectors for enhanced performance and improved *in-situ and operando* capabilities

In the previous section we have discussed the advantages of using a VCO as a compact device for pulsed EPR experiments, capable of generating short and strong microwave pulses and, at the same time, being able to sense the spins' response in a deadtime-free manner. One crucial requirement of pulsed EPR, which has not been discussed so far, is the need for a highly homogeneous B_1 field over the entire sample volume [22]. This is because the magnetic moment vectors of two spins experiencing excitation pulses of identical duration and frequency but different B_1 magnitudes will be rotated by different flip angles, in general leading to a reduced net change of the total sample magnetization vector. The situation is even worse for multi-pulse experiments, in which, instead of a single pulse, a series of microwave pulses is exploited to increase the information content of the EPR signal for measuring, e.g., the sample's relaxation times [23], or the distance between paramagnetic centers in proteins [24]. A high B_1 homogeneity is also important when designing shaped pulses [22], i.e. pulse with an envelope and phase other than the classical block pulses, to maximize the excitation bandwidth. For the planar on-chip coils used in all EPRoC chips presented so far, the B_1 component in the direction perpendicular to the chip surface (B_{1z}) decays quickly, while, especially close to the coil trace, there is a strong undesired lateral B_1 component ($B_{1x,y}$), depending on the direction of the B_0 along the y- and x-axis, respectively. This introduces a hard trade-off for the conventional placement of samples inside a capillary parallel to the chip surface between sensitivity and B_1 homogeneity. More specifically, to maximize the field homogeneity, a thin capillary with a certain distance to the chip surface should be used to minimize the change in B_{1z} across the sample. However, this configuration drastically reduces the usable sample volume and detector fill factor, leading to a severe loss of signal and eventually sensitivity [6]. To break this

trade-off, we propose to create a hole within the VCO coil to enable a mounting of cylindrical capillaries through the on-chip detector. This allows for the placement of the sample within the most sensitive and homogeneous region of the EPRoC sensor. In order to compare the conventional and the proposed method, we have performed extensive electromagnetic (EM) simulations of the B_1 distribution over the sample volume in the case of parallel-mounted rectangular capillaries, and the case of through-hole-mounted cylindrical capillaries. Here, for the former case, we have modeled the sample as a cuboid with a volume of $200 \times 200 \times 100$ μm placed 24 μm above the coil surface, taking into account the 3 μm-thick passivation layer of the CMOS chip, and the 21 μm wall thickness of a commercial capillary (VitroCom 5003). For the latter case, we have used the geometry parameters (outer diameter of 120 μm, inner diameter of 82 μm) of a commercial capillary offered by Hilgenberg GmbH. The simulation models and results are presented in Figure 14. According to Figure 14c and d, the B_1 field inside the cylindrical capillary has significantly reduced undesirable B_{1x} components than the one inside the rectangular capillary. By post-processing the data of Figure 14c and d, we computed the volume-averages of the field components $\overline{B_{1z}}$ and $\overline{B_{1x}}$, as well as the corresponding standard deviation σ_{B1z} of B_{1z}. From this, we define the field inhomogeneity as the normalized standard deviation of the B_{1z} field according to $\frac{\sigma_{B1z}}{|\overline{B_{1z}}|}$. Table 1 summarizes the corresponding results, clearly showing an improved amplitude of the B_0 field by 1.5×, an improved homogeneity by 2×, and a reduced lateral field by 6× of the proposed capillary mounting through the tank coil of the EPRoC detector.

Although the proposed solution of drilling a hole through the on-chip coil is straightforward in theory, in practice, many drilling methods introduce a large number of the so-called dangling bond defects at the exposed semiconductor surface, which display a strong EPR signal [25]. To minimize the creation of such defects, we have compared two methods for creating the required hole, laser drilling and focused ion beam (FIB) milling, in terms of precision, drill time, and the quality of the resulting hole surface. We found that using a pulsed picosecond laser source with a wavelength of 532 nm (Duetto S/N 184 from Rofin), a hole diameter of 100–200 μm can be drilled through a 50 μm thick silicon substrate in a very short time of several seconds, while a similarly sized hole needs several hours of drill time using FIB milling. Laser drilling, however, produces a less precise hole and affects the surrounding circuitry. As shown in Figure 15a, the perimeter of a laser-drilled hole contains a 20 μm-wide ring of overheated silicon that affects the surrounding circuitry. In contrast, a well-defined hole of
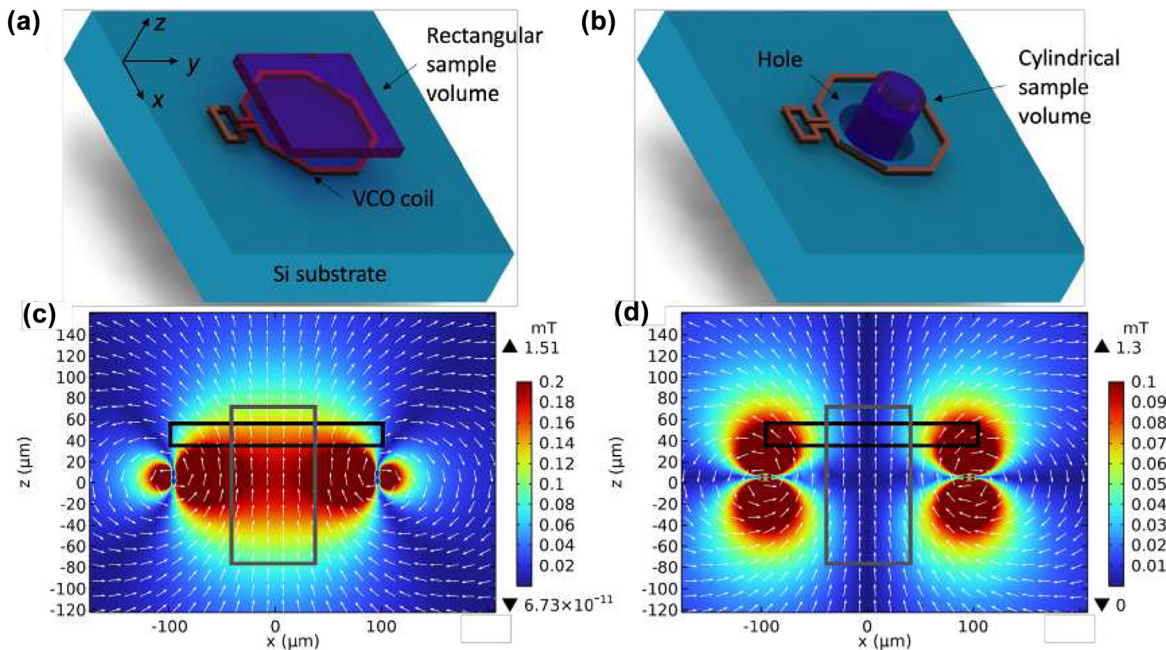
Figure 14: Finite-element method simulations for different placements of the sample. (a) and (b): Simulation models in COMSOL corresponding to parallel and perpendicular capillary placements, respectively. (c) and (d) Field distributions respectively of the B_{1z}, and B_{1x} components in an xz-cross plane through the coil center when an RF current of 30 mA runs inside the coil. The arrow fields in (c) and (d) represent the direction of the normalized B_1 field. The black and gray rectangles in (c) and (d) represent the sample volumes as placed in panes (a) and (b).

Table 1: Simulated results of two capillary placement methods as shown in Figure 14.

	Rectangular capillary	Cylindrical capillary	Improvement factor
$\left\|\overline{B_{1z}}\right\|$	0.11 mT	0.16 mT	1.5×
$\left\|\overline{B_{1x}}\right\|$	0.06 mT	0.01 mT	6×
σ_{B1z}	0.04 mT	0.03 mT	
$\frac{\sigma_{B1z}}{\left\|\overline{B_{1z}}\right\|}$	44%	21%	2×

118 μm size created by FIB milling (Crossbeam 340, current of 100 nA) is shown in Figure 15b. Here, it should be noted

that a part of the lack in precision of the laser-drilled holes can be attributed to the lack of a high resolution integrated microscope in our laser system. Overall, FIB milling is capable of generating precisely positioned holes through the on-chip inductors with a well-defined shape, at the expense of very long (several hours per hole) milling times.

To verify that FIB milling does not introduce a significant amount of dangling bond defects, we have conducted field-swept CW EPR experiments with the FIB-processed chip. Here, first, we have measured a sample of 10 mm of TEMPOL (4-hydroxy-TEMPO, Sigma Aldrich) in deionized water inside a 0.12 μm outer diameter cylindrical capillary (Hilgenberg GmbH) mounted through the chip hole. The
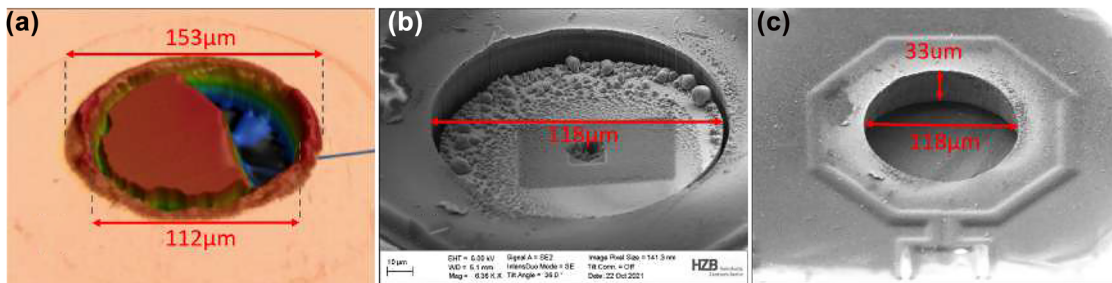

Figure 15: Results of drilling using different techniques. (a) Image of a hole created by laser drilling, (b) SEM image of the a hole on a 14 GHz chip after FIB milling, and (c) the same FIB-milled hole after a last sonication and washing step. The VCO coil in shape of a hexagon can be seen around the milled hole.

corresponding results are shown in Figure 15a (blue). Then, we removed the capillary and measured the background EPR signal from the dangling bond defects. The corresponding results shown in Figure 15b (red) indicate that there is no noticeable background signal, confirming the very small amount of created defects. Moreover, the concentration sensitivity extracted from the TEMPOL measurement is $450\,\mu M/\sqrt{Hz}$, which is on par with state-of-the-art EPRoC detectors [9], verifying that the hole drilling process does not affect the chip performance. The negligible effect of the hole drilling process on the chip performance was also verified by electrical measurements of the chip's phase and frequency noise floor shown in Figure 16b. The measured phase noise is virtually unchanged by the drilling and on par with the state-of-the-art single-VCO EPRoC detectors.

In summary, we have investigated different options for creating a hole through the coils of EPRoC detectors,

identifying FIB as a viable option for high-precision holes with minimum chip damage. The negligible effect of the FIB milling on the chip performance was verified by electrical and EPR measurements.

8 Sample delivery system

8.1 Overview

For a wide adoption of CMOS-based EPRoC detectors, a sample delivery system allowing for the reusability of both the ASIC and the sample is crucial. One possible approach is to deliver the sample via a fluidic network through a hole in the ASIC, schematically shown in Figure 17a. In this way, the sample can be recovered and the ASIC reused after cleaning the fluidic network with an appropriate solvent.
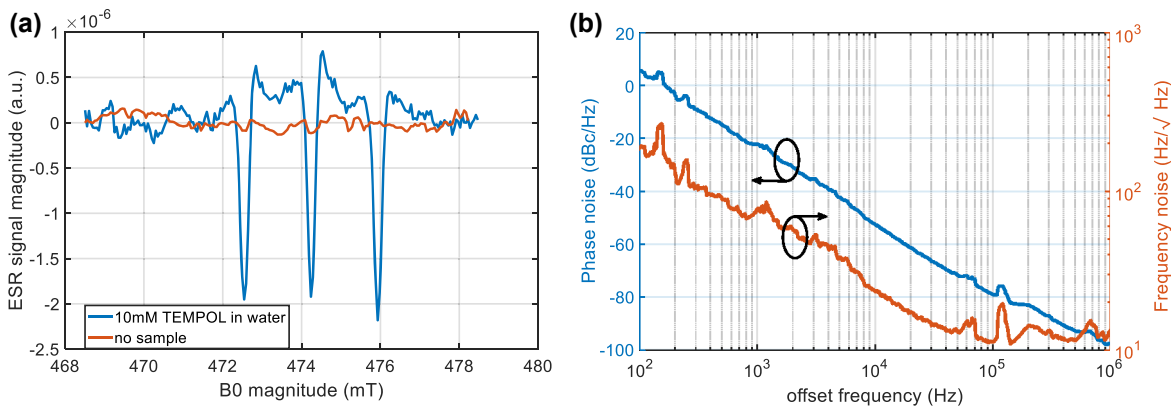

Figure 16: Measurements of the chip after drilling. (a) Measured EPR signals with and without a dedicated sample, (b) measured phase and frequency noise of the FIB-milled VCO.
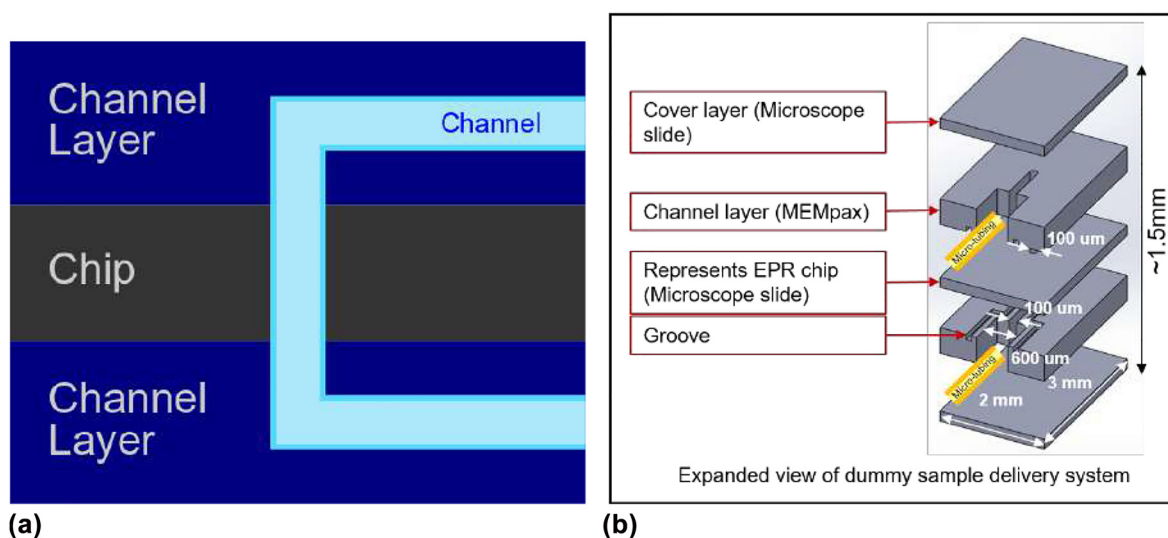

Figure 17: Illustrations of the proposed sample delivery system. (a) Schematic representation of the sample delivery system. (b) Expanded view of the sample delivery system prototype.

To produce such a sample delivery system, which is compatible with the target EPR application, a non-magnetic material devoid of an EPR background signal is necessary. Glass is an excellent choice, with the added benefit of being largely chemically inert. The challenge is in manufacturing 3D glass components at dimensions compatible with the EPRoC detector.

8.2 Sample delivery through the VCO coil

The proposed sample transport systems consists of a five-layer assembly. The EPRoC device being the middle layer, sandwiched between two-layer fluidic transport devices contacted both above and below the ASIC to deliver the sample through the VCO coil. To prototype this concept, we tested a dummy device consisting of fluidic transport layers (first, second, fourth, and fifth layers) together with a glass slide cut in the expected dimensions of the EPRoC device (third layer), schematically shown in Figure 17b. Here, we quickly noted that fixing the layers and attaching the tubing transporting the sample to and from the system such that the fluidic path was unobstructed, while the entire assembly was sealed and free of leaks, required an update in the design concept. The key was to include a trench cut into the fluidic top and bottom pieces that would accommodate the ASIC, aiding in the alignment of the fluidic path. Another challenge was finding a suitable sealing agent, and after screening a variety of epoxies, a two-component epoxy by UHU GmbH & Co. KG was selected. By incorporating these improvements, we could demonstrate sample transport in a fully sealed dummy device, cf. Figure 18.

8.3 Monolithic fluidic transport devices

Starting from the first prototype design discussed in the previous sections, we simplified the design by using monolithic top and bottom fluidic delivery devices (schematic in Figure 19) and fabricated them in glass, hereafter referred to as glass chips. An important feature of the glass chip was a rectangular volume cut from the side to accommodate access to the wirebond pads on the ASIC after assembly. Together with the well holding the EPRoC device, the length of the bond wires can be minimized to reduce deleterious effects on MW performance. The tolerances of the rectangular well to hold the EPRoC device were kept such that the channel-hole-channel alignment could be achieved even in the case of misalignment of the individual pieces. The height of the rectangular well walls holding the EPRoC device is a critical dimension; given the target ASIC thickness of 50 μm, the wall height on each glass-chip could not be more than 25 μm. This fabrication requirement was a challenge; however, using the laser-machining process offered by LightFab GmbH, we were able to manufacture a final glass chip that meets the above-mentioned specifications, cf. Figure 20.
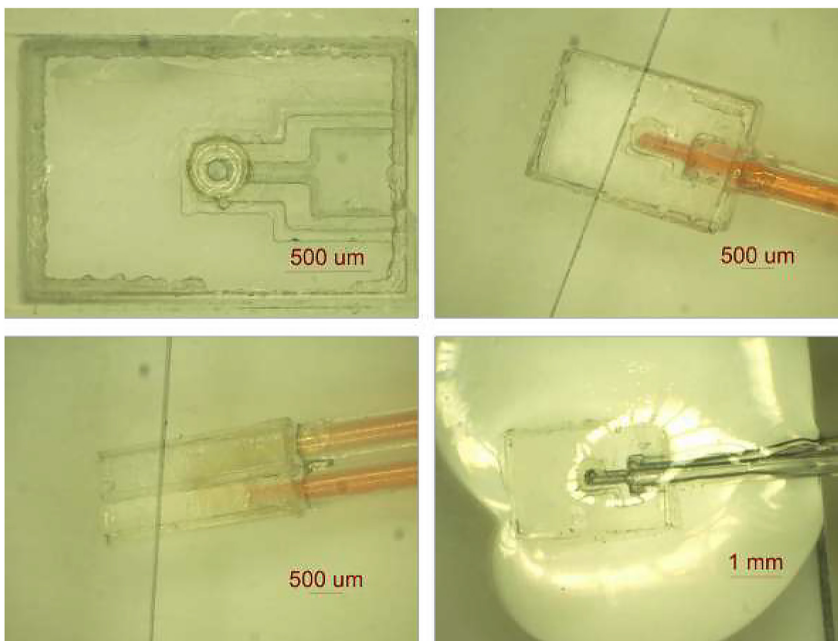

Figure 18: Functioning prototype of the sample delivery system formed by five glass layers (see Figure 17b). Red colored water is used to test liquid flow in the system, highlighting transport through the entire fluidic path. In addition, after submerged in water with air passed through the channels, no bubbles are observed confirming a leak-free assembly (bottom right).
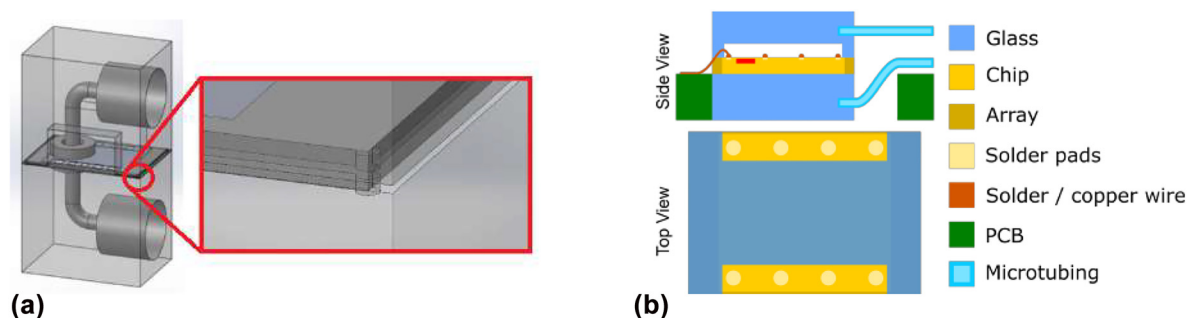
Figure 19: Integration of the EPRoC chip in the microfluidic device. (a) Schematic of the final glass chip design with the EPRoC ASIC sandwiched between them. Channels in the glass-chips self-align with the hole in the ASIC to form a continuous channel. (b) Illustration of the sample delivery system including PCB mounting. The bottom glass chip is placed in a groove within the PCB. This enables the shortest bond wires possible to optimize MW performance.
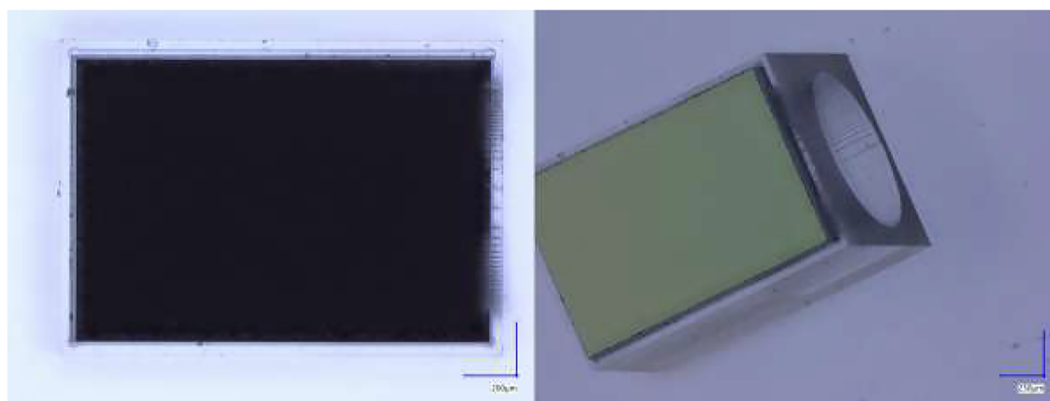

Figure 20: Photographs of a silicon chip placed in the rectangular cutout of a first generation fabricated glass chip; top view (left), isometric view (right). The cutout is designed for easy alignment of the channel-hole-channel of the sample delivery system. The cylindrical cutout visible in the isometric view of the glass chip will be used for microtubing which connects the fluidic network of the EPRoC device to the outside world.

9 Portable magnet for EPR

9.1 Overview

Portable EPR systems naturally require compact magnets. By contrast, commercially available EPR systems use bulky electromagnets capable of producing the required magnetic field strengths, but preventing portability. For Ka-band EPR, the required field strength is between 0.9 and 1.3 T, now achievable with permanent magnets. With the advancement of permanent magnetic materials (e.g. neodymium-based magnets such as (NdFeB) [26]) an EPR magnet with sufficient field strength and homogeneity can be designed. In fact, commercial benchtop NMR systems take advantage of permanent magnet designs, where the constraints on field homogeneity are even more demanding than in EPR [27].

An optimized Halbach cylindrical structure made from permanent magnets (NdFeB) produces the strongest homogeneous field possible per used magnet mass [28–30], and can achieve the desired homogeneity at around room temperatures [31]. Regarding the choice on the shape of the magnet unit cells, several options have been proposed in the literature. Blümler and co-workers have used magnets with both circular and square cross sections to reduce the production-induced magnetic field direction heterogeneity [32]. An alternative geometry is wedge shaped discrete magnets, which reduce the non-magnetic gap between adjacent magnets in the structure and in turn reduce stray magnetic field. In addition, this geometry yields a higher achievable field strength for a given amount of magnetic material [33]. In his original papers, Halbach suggests that for a dipole structure eight magnets per layer structure should be sufficient to cancel individual magnet non-uniformities [31, 34, 35]. Taking the manufacturing inhomogeneities into consideration, in this paper, we propose to use 16 wedge-shaped magnets per layer.
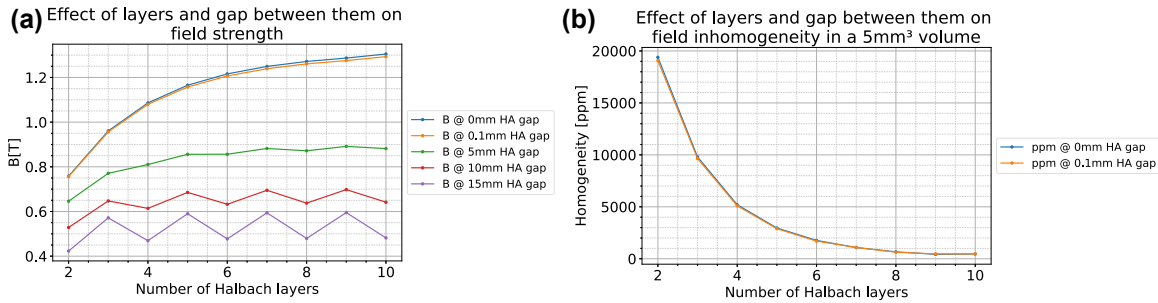
Figure 21: Simulations of the proposed permanent magnet performed using COMSOL Multiphysics. (a) Influence of the number of Halbach layers and the gap between them on the effective magnetic field strength of the assembly. (b) Influence of the gap between the Halbach layers on the magnet field homogeneity of the assembly. The field homogeneity was calculated in a 5 mm cube in the center of the assembly.

9.2 Permanent magnet design–Simulation results

To rationalize the design, we performed simulations in COMSOL Multiphysics with the intention to build a Halbach structure for EPR with 16 discrete, wedge shaped magnets in each layer. The dimensions of the magnetic structure were optimized to produce a B_0 field of ≈1.2 T with the highest homogeneity at the center. Each individual magnet piece was 10 mm in height, the diameter of the Halbach structure was 89 mm, the minimum diameter at the center (volume of interest) was 23.5 mm, and a total of ten layers were used. The resulting mass would be ≈3.85 kg. The generated magnetic field strength can be controlled by varying the number of layers and the width of the gaps between them, cf. Figure 21a. This also varies the homogeneity of the generated magnetic field, cf. Figure 21b. For these simulations, we used a nonlinear B-H-curve with a remnant B field of 1.2 T.

The presented simulation results indicate that a compact permanent magnet for Ka-band EPR can be designed. By varying the number of layers in the assembly, the magnetic field can be tuned to the operating frequency of the EPRoC detector. If necessary, the field homogeneity could be improved by incorporating additional shim structures into the Halbach design.

10 Conclusion and outlook

In this paper, we have presented our recent progress towards VCO-based EPR-on-chip detectors for in-cell EPR applications. After a brief introduction into conventional EPR and a short summary of the current state-of-the-art in VCO-based EPR-on-a-chip detectors, we have presented a scheme for pulsed EPR detection using chip-integrated VCOs for both the excitation and the dead time-free detection of the resulting EPR signal. Together with the scheme, we have presented an analytical model for pulsed VCO-based EPR experiments. Both the proposed experimental scheme and the analytical model have been validated using a custom-designed Ka-band EPRoC detector. Furthermore, we have presented an approach for homogenizing the B_1 field of the chip-integrated EPR detectors by drilling a hole through the silicon chips. A comparison of different hole-drilling methods showed that FIB milling can be used to produce the required holes with high precision, no noticeable chip damage and minimum dangling bond defects. In the future, we will combine the presented EPRoC detector with the through-hole with the microfluidic devices discussed in Section 8 of this paper. Finally, we have presented our progress towards miniaturized EPR magnets, which will pave the way towards portable EPR systems, greatly extending the application range of today's EPR systems. As our next steps, we will investigate the possibility of performing multi-pulse experiments, including DEER-type EPR, with the VCO-based detectors to enable distance measurements within single cells. Furthermore, we will perform additionally investigations on the signal intensity dependence of the EPR signals at the VCO's AM and FM output as a function of offset frequency. Finally, we will assemble a complete portable pulsed EPR spectrometer by combining the presented EPRoC detectors with the microfluidic devices for sample handling and the small-sized permanent magnets.

Author contributions: All the authors have accepted responsibility for the entire content of this submitted manuscript and approved submission.
Conflict of interest statement: J.G.K. is a shareholder of Voxalytic GmbH, a company that markets miniaturized NMR equipment. The other authors declare no conflicts of interest.

References

[1] J. Yang, Y. Wang, Z. Wang, et al., "Observing quantum oscillation of ground states in single molecular magnet," *Phys. Rev. Lett.*, vol. 108, p. 230501, 2012.

[2] A. Matsumura, M. C. Emoto, S. Suzuki, et al., "Evaluation of oxidative stress in the brain of a transgenic mouse model of alzheimer disease by in vivo electron paramagnetic resonance imaging," *Free Radic. Biol. Med.*, vol. 85, pp. 165–173, 2015.

[3] M. Azarkh, A. Bieber, M. Qi, et al., "Gd(iii)–Gd(iii) relaxation-induced dipolar modulation enhancement for in-cell electron paramagnetic resonance distance determination," *J. Phys. Chem. Lett.*, vol. 10, no. 7, pp. 1477–1481, 2019.

[4] S. J. Fries, T. S. Braun, C. Globisch, C. Peter, M. Drescher, and E. Deuerling, "Deciphering molecular details of the rac–ribosome interaction by epr spectroscopy," *Sci. Rep.*, vol. 8681, 2021, https://doi.org/10.1038/s41598-021-87847-y.

[5] M. Toybenshlak and R. Carmieli, "Monitoring metallic sub-micrometric lithium structures in Li-ion batteries by in situ electron paramagnetic resonance correlated spectroscopy and imaging," *Nat. Commun.*, vol. 1410, 2021.

[6] T. Yalcin and G. Boero, "Single-chip detector for electron spin resonance spectroscopy," *Rev. Sci. Instrum.*, vol. 79, no. 9, p. 094105, 2008.

[7] J. Anders, "Fully-integrated CMOS Probes for Magnetic Resonance Applications," Ph.D. thesis, École polytechnique fédérale de Lausanne, Lausanne, Switzerland, 2011.

[8] J. Handwerker, B. Schlecker, U. Wachter, P. Radermacher, M. Ortmanns, and J. Anders, "A 14 GHz battery-operated point-of-care ESR spectrometer based on a 0.13 μm CMOS ASIC," in *2016 IEEE International Solid-State Circuits Conference (ISSCC)*, New Jersey, USA, Institute of Electrical and Electronics Engineers, 2016, pp. 476–477.

[9] A. Chu, B. Schlecker, K. Lips, M. Ortmanns, and J. Anders, "An 8-channel 13 GHz ESR-on-a-chip injection-locked VCO-array achieving 200 μM-concentration sensitivity," in *2018 IEEE International Solid – State Circuits Conference – (ISSCC)*, New Jersey, USA, Institute of Electrical and Electronics Engineers, 2018, pp. 354–356.

[10] B. Schlecker, A. Hoffmann, A. Chu, M. Ortmanns, K. Lips, and J. Anders, "Towards low-cost, high-sensitivity point-of-care diagnostics using VCO-based ESR-on-a-chip detectors," *IEEE Sensor. J.*, vol. 19, no. 20, pp. 8995–9003, 2019.

[11] M. A. Hassan, T. Elrifai, A. Sakr, M. Kern, K. Lips, and J. Anders, "A 14-channel 7 GHz VCO-based EPR-on-a-chip sensor with rapid scan capabilities," in *2021 IEEE Sensors*, New Jersey, USA, Institute of Electrical and Electronics Engineers, 2021, pp. 1–4.

[12] M. Toybenshlak and R. Carmieli, "A new and robust method for in-situ EPR electrochemistry," *Isr. J. Chem.*, vol. 59, nos. 11–12, pp. 1020–1026, 2019.

[13] J. Guo, X. Luan, Y. Tian, et al., "The design of X-band EPR cavity with narrow detection aperture for in vivo fingernail dosimetry after accidental exposure to ionizing radiation," *Sci. Rep.*, vol. 2883, 2021, https://doi.org/10.1038/s41598-021-82462-3.

[14] G. J. A. Schweiger, *Principles of Pulse Electron Paramagnetic Resonance*, New York, Oxford University Press, 2001.

[15] J. Anders, "Nonlinear modeling of continuous-wave spin detection using oscillator-based ESR-on-a-chip sensors," in *Recent Advances in Nonlinear Dynamics and Synchronization: With Selected Applications in Electrical Engineering, Neurocomputing, and Transportation*, K. Kyamakya, W. Mathis, R. Stoop, J. C. Chedjou, and Z. Li, Eds., Cham, Springer International Publishing, 2018, pp. 57–87.

[16] A. Chu, B. Schlecker, M. Kern, et al., "On the modeling of amplitude-sensitive electron spin resonance ESR detection using voltage-controlled oscillator VCO-based ESR-on-a-chip detectors," *Magn. Reson.*, vol. 2, no. 2, pp. 699–713, 2021.

[17] S. Künstner, A. Chu, K.-P. Dinse, et al., "Rapid-scan electron paramagnetic resonance using an EPR-on-a-chip sensor," *Magn. Reson.*, vol. 2, no. 2, pp. 673–687, 2021.

[18] A. Chu, B. Schlecker, J. Handwerker, et al., "VCO-based ESR-on-a-chip as a tool for low-cost, high-sensitivity food quality control," in *2017 IEEE Biomedical Circuits and Systems Conference (BioCAS)*, New Jersey, USA, Institute of Electrical and Electronics Engineers, 2017, pp. 1–4.

[19] A. Chu, B. Schlecker, and J. Anders, "Transistor-level simulation of LC-tank vco electron spin resonance detectors," in *ANALOG 2018; 16th GMM/ITG-Symposium*, New Jersey, USA, Institute of Electrical and Electronics Engineers, 2018, pp. 1–2.

[20] S. Pribitzer, A. Doll, and G. Jeschke, "Spidyan, a MATLAB library for simulating pulse EPR experiments with arbitrary waveform excitation," *J. Magn. Reson.*, vol. 263, pp. 45–54, 2016.

[21] S. Stoll and A. Schweiger, "Easyspin, a comprehensive software package for spectral simulation and analysis in EPR," *J. Magn. Reson.*, vol. 178, no. 1, pp. 42–55, 2006.

[22] P. E. Spindler, Y. Zhang, B. Endeward, et al., "Shaped optimal control pulses for increased excitation bandwidth in EPR," *J. Magn. Reson.*, vol. 218, pp. 49–58, 2012.

[23] S. Stoll, *Pulse EPR*, New Jersey, USA, John Wiley & Sons, Ltd, 2017, pp. 23–38.

[24] G. Jeschke, "Deer distance measurements on proteins," *Annu. Rev. Phys. Chem.*, vol. 63, no. 1, pp. 419–446, 2012.

[25] B. P. Lemke and D. Haneman, "Dangling bonds on silicon," *Phys. Rev. B*, vol. 17, pp. 1893–1907, 1978.

[26] M. Sagawa, S. Fujimura, H. Yamamoto, Y. Matsuura, and K. Hiraga, "Permanent magnet materials based on the rare earth-iron-boron tetragonal compounds," *IEEE Trans. Magn.*, vol. 20, no. 5, pp. 1584–1589, 1984.

[27] E. Keiji, "JEOL, NMR and ESR: a 65 year evolution," *J. Magn. Reson.*, vol. 306, pp. 17–26, 2019.

[28] V. Samofalov, D. Belozorov, and A. Ravlik, "Optimization of systems of permanent magnets," *Phys. Met. Metallogr.*, vol. 102, no. 5, pp. 494–505, 2006.

[29] J. Jensen and M. Abele, "Erratum:maximally efficient permanent magnet structures," *J. Appl. Phys.*, vol. 80, no. 3, p. 1941, 1996.

[30] M. L. Johns, E. O. Fridjonsson, S. J. Vogt, and A. Haber, *Mobile NMR and MRI: Developments and Applications*, London, UK, Royal Society of Chemistry, 2015.

[31] K. Halbach, "Design of permanent multipole magnets with oriented rare earth cobalt material," *Nucl. Instrum. Methods*, vol. 169, no. 1, pp. 1–10, 1980.

[32] H. Raich and P. Blümler, "Design and construction of a dipolar Halbach array with a homogeneous field from

identical bar magnets: NMR Mandhalas," *Concepts Magn. Reson. Part B: Magn. Reson. Eng: Educ. J.*, vol. 23, no. 1, pp. 16–25, 2004.

[33] M. Abele, "Generation of highly uniform fields with permanent magnets," *J. Appl. Phys.*, vol. 76, no. 10, pp. 6247–6252, 1994.

[34] K. Halbach, "Strong rare earth cobalt quadrupoles," *IEEE Trans. Nucl. Sci.*, vol. 26, no. 3, pp. 3882–3884, 1979.

[35] K. Halbach, "Physical and optical properties of rare earth cobalt magnets," *Nucl. Instrum. Methods Phys. Res.*, vol. 187, no. 1, pp. 109–117, 1981.